THE ASTROPHYSICAL JOURNAL, 527:415–425, 1999 December 10
© 1999. The American Astronomical Society. All rights reserved. Printed in U.S.A.

MICROWAVE AND EXTREME ULTRAVIOLET OBSERVATIONS OF SOLAR POLAR REGIONS

A. NINDOS, M. R. KUNDU, AND S. M. WHITE
Astronomy Department, University of Maryland, College Park, MD 20742
D. E. GARY
Physics Department, NJIT, Newark, NJ 07102
K. SHIBASAKI
Nobeyama Radio Observatory, Minamimaki, Minamisaku, Nagano 384-13, Japan
AND
K. P. DERE
Naval Research Laboratory, Code 7663, Washington DC 20375
Received 1999 March 19; accepted 1999 July 16

ABSTRACT

The poles of the Sun are brighter than the rest of the quiet Sun's emission in a limited range of radio frequencies from 17 GHz to 87 GHz. We have studied microwave images of the quiet Sun made with the Nobeyama radioheliograph at 17 GHz. They show that the so-called polar-cap brightening consists of two components: a diffuse component of 1500 K excess brightness and patchy compact sources with localized excess brightness of about 3500 K. We test the reality of the compact sources using the maximum entropy method deconvolution. The total flux and the number of compact polar sources as well as the north-south extent of the diffuse polar emission are larger in the pole that is closest to the Earth. We compared the microwave polar emission with nearly simultaneous *SOHO* EIT images taken in the lines of He II at 304 Å and Fe XII at 195 Å. No one-to-one correlation between the compact radio sources and the bright EUV features was found: most of the radio emission arises between the plumes visible to EIT. The boundaries of the polar-cap brightenings did not match exactly the boundaries of the coronal holes as seen in either the Fe XII 195 Å images or the He II 304 Å images. The temporal variations of the compact microwave sources did not correspond to any significant changes in EUV emission. On the other hand, most He II 304 Å changing features were associated with the diffuse polar microwave emission, which was practically constant. Our data suggest that the origin of the polar brightening is not coronal; it seems that the bulk of the patchy radio emission comes from heights below the 80,000 K layer.

Subject headings: Sun: corona — Sun: radio radiation — Sun: UV radiation

1. INTRODUCTION

The polar regions of the Sun have a low-density atmosphere that makes the Sun appear dark there in virtually all wavelengths at which images of the Sun are taken. However, radio observations have revealed the remarkable result that the polar regions of the Sun are brighter than the rest of the quiet Sun in a limited range of frequencies from 17 GHz to about 87 GHz. The first such report of polar brightening was published by Kundu & McCullough (1972), who observed a polar brightness excess at 31 GHz associated with a coronal hole. Babin et al. (1976) explicitly addressed the issue of the so-called polar-cap brightenings using the Crimean 22 m Telescope at frequencies of 22 and 37 GHz with an angular resolution of 1′–2′. They found that polar-cap brightenings have a maximum east-west extent of 2′ and excess brightness temperatures of 1500 and 800 K at 22 GHz and 37 GHz, respectively. Efanov et al. (1980a, 1980b) reported that polar-cap brightenings at 22 and 37 GHz were absent between 1968–1972 but appeared and persisted following the maximum phase of solar activity in 1972. More recently, Riehokainen, Urpo, & Valtaoja (1998) showed that the yearly variation of the number of polar-cap brightenings at 37 GHz does not follow the sunspot cycle. Kosugi, Ishiguro, & Shibasaki (1986) used the 45 m Nobeyama radiotelescope and confirmed the presence of a 3%–7% brightness excess in polar regions at 36 GHz but found no such excess at 96 GHz. They also found that at 36 GHz, polar coronal holes always showed an excess brightening while only half of the equatorial coronal holes did. Pohjolainen et al. (1998) reported polar radio brightness temperature enhancements at frequencies as high as 87 GHz. Koshiishi (1996) developed a deep-clean imaging method and applied it to Nobeyama radioheliograph (NRH) 17 GHz data. He found that beyond 0.95 $R_\odot$, patchy brightenings more than 2000 K above the average quiet-disk brightness are often present. At frequencies lower than 10 GHz, the poles are usually darker than the quiet Sun because of a deficit of coronal material associated with the polar coronal holes.

Explanations proposed for the anomalous brightening are that it may be related to a lower gradient of density and temperature in the transition region of coronal holes compared with average quiet regions or to a wider temperature plateau in the upper chromosphere (Hiei 1987). Koshiishi (1996) noted an association between the solar cycle variation of the brightening and similar variation in polar magnetic fields and polar white-light faculae. Alternatively, Riehokainen et al. (1998) speculated that it may be associated with density and temperature enhancements of polar network elements. Recent EIT observations have shown that "the more carefully we look for the quiet Sun, the harder it is to find" (Berghmans, Clette, & Moses 1998). Thus another explanation might be that the excess radio brightening in the polar regions reflects the summation of

random brightenings associated with plume or interplume regions.

These radio polar cap brightenings must be the result of the structure of the solar atmosphere at the poles and thus have the potential to be a valuable diagnostic for the polar regions. In this paper, we study the properties of the radio polar-cap brightenings using high-resolution observations at 17 GHz from NRH. These data have the advantage that the brightening is relatively prominent at 17 GHz, the spatial resolution of the data is excellent, images are available every day since 1992, and the data are well calibrated. Nearly simultaneous EUV observations from *SOHO* EIT provide additional information on the state of the transition region and/or coronal polar plasma.

We remind the reader that the mechanism that dominates quiet Sun's millimeter and microwave emission is thermal bremsstrahlung (free-free mechanism). The Sun's atmosphere is optically thick to bremsstrahlung at a height that decreases as frequency increases: at about the 10,000 K level at 17 GHz and 7000 K at 86 GHz. The contribution from optically thin coronal emission is generally small in the quiet Sun (and smaller at 86 GHz than at 17 GHz). On the other hand, the intensities of the EUV Fe XII and He II lines are dependent on the amounts of material at about 10^6 and 10^5 K, respectively. Thus the 304 Å EIT images show the chromospheric network structure of the quiet Sun, while the 195 Å images reveal the corona. A comparison of the radio data with the EIT images should help us to derive a more comprehensive picture of this, so far, unexplained phenomenon.

One particular aspect on which we focus is the possibility that the radio polar brightening is related to activity observed in polar plumes. These are open-field high-density structures in the polar coronal holes that are stable over long timescales but which show considerable activity at their base on timescales of minutes (DeForest et al. 1997; DeForest, & Gurman 1998). This property suggests that a recurring brightening and injection of cool material at a number of compact sites spread through the low corona may show up as a polar brightening at radio wavelengths, and we look for such properties in the radio emission.

2. DATA ANALYSIS

We chose 19 days close to solar minimum when the Sun was generally quiet for a detailed study of the polar-cap brightening. The NRH observations at 17 GHz were made with a spatial resolution of $\sim 15''$. The NRH records both right-handed and left-handed circular polarization. Its field of view covers the entire Sun, and it has a dynamic range better than 25 db (Koshiishi et al. 1994). The NRH is a large T-shaped array that consists of 84 antennas whose spacings are all multiples of a fundamental unit. This was done deliberately so that redundant spacing information could be used in calibration, but it also means that the snapshot dirty beam has large sidelobes. For example, if we map the calibrated visibilities with a cell size of 4.″4 (this is the value we used for the computation of the maps presented in this paper), the instantaneous dirty beam (i.e., the telescope response to a point source; the raw maps are the convolution of the sky brightness distribution with the dirty beam) shows strong sidelobes approximately every 155″ that reach half the intensity of the beam's peak. The large sidelobes make the mapping of weak diffuse features, like the polar brightening, difficult over short time intervals.

In order to determine the sky brightness distribution we must deconvolve the dirty beam from the raw maps. There is no unique solution to the deconvolution problem, and different techniques have different properties. Features that recovered by several different deconvolution methods are more likely to be real. In order to study the reality of the compact polar sources, we compared snapshot full-disk maps produced by different restoration techniques. We tried, within AIPS, the standard CLEAN algorithm, the so-called Steer CLEAN algorithm (Steer, Dewdney, & Ito 1984), and the maximum entropy method (MEM). Since the MEM algorithm has not been widely applied to NRH data, we compare it with the CLEAN and Steer deconvolutions for a model image in Appendix A. We found that, although all of the methods can produce small-scale artifacts in smooth areas, the MEM always gave significantly better results than either CLEAN method. The MEM method has better response to weak extended structures than the more usual CLEAN procedure and permits higher dynamic range, which is necessary for the analysis of low-brightness solar phenomena. Using MEM, we produced full disk maps at 17 GHz, corresponding approximately to the times of the EIT images of our collection. In Table 1 we give the time intervals and the temporal resolution of the radio and EUV data sets that we studied. The EIT images (Delaboudinière et al. 1995) were flat-fielded, degridded, background-subtracted, and exposure-time–normalized using the standard calibration software.

An important task is to align accurately the NRH and the EIT images. The pixel size we used to make the NRH images was 4.″4 while the EIT pixel size is 2.″62 (Delaboudinière et al. 1995). The limb in the 17 GHz images is well determined, at 1.0125 solar radii (i.e., a height of 8700 km above the photosphere). We found that the emission limb in the He II 304 Å images was always larger than the limb in the NRH images. The range of the differences between the height of the limb in the 304 Å images and the height of the 17 GHz limb was from about 5500 km up to

TABLE 1

NRH AND EIT OBSERVATIONS

Date (1997)	Time (UT)	EIT Wavelengths (Å)	Time Resolution (minutes)
March 2–March 7	1:00–3:30	195,304	15
March 11–March 13.....	1:00–3:30	195,304	15
March 15–March 17.....	1:00–3:30	195,304	15
March 19	0:00–6:20	304	7
May 29–May 30	22:30–23:30	195	1
June 2	22:30–23:30	195	1

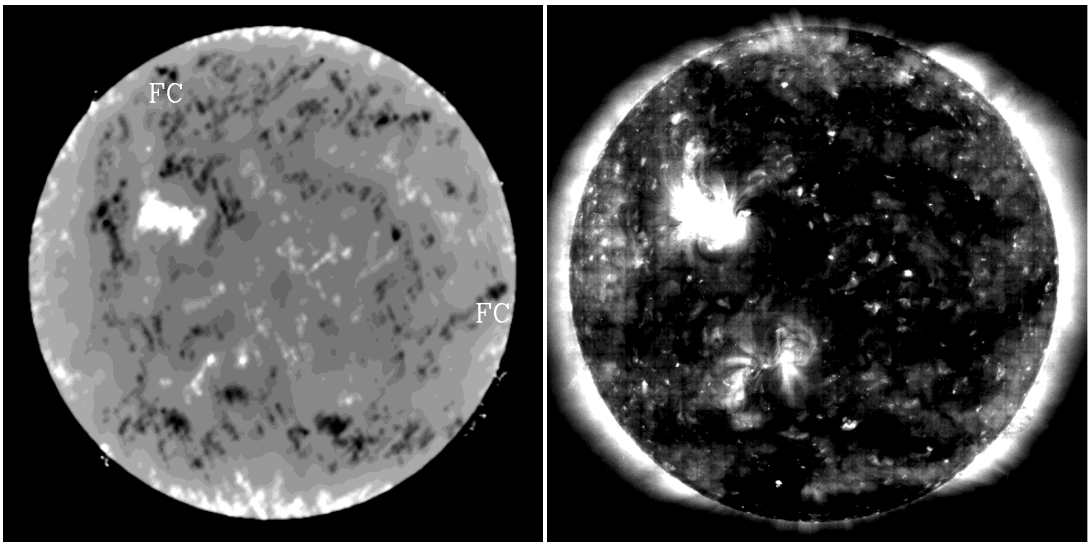

FIG. 1.—Nobeyama 17 GHz and EIT 195 Å observations of the Sun on 1997 March 11. The gray-scale range is chosen to emphasize the structure at the poles: in the 17 GHz image it ranges from 8000 K to 12,500 K in brightness temperature. The labels "FC" mark the filament channels that we discuss in § 4.

7900 km at the poles. Our measurements confirmed the results of Zhang, White, & Kundu (1998), who studied another data set of EIT images and found that the limb is higher at the poles than at the equator. This asymmetry has been also observed in Hα images (Johannesson, & Zirin 1996). When possible, our co-alignment was also checked by comparing the extended emission associated with small active regions that were visible at both radio and EUV wavelengths. We are confident that the uncertainty of the coalignment is less than one EIT pixel.

3. BASIC PROPERTIES OF THE 17 GHZ POLAR CAP BRIGHTENINGS

We illustrate the properties of the polar-cap brightenings in Figures 1, 2, and 3. A comprehensive discussion of the properties is given by Koshiishi (1996). Figure 1 shows nearly simultaneous snapshot images of the Sun on 1997 March 11 at 17 GHz and in the Fe XII 195 Å EIT filter. The polar brightening is immediately evident in the 17 GHz image as the brightest feature on the disk apart from an active region; there are times during solar minimum when the poles are the brightest features on the Sun at 17 GHz. To quantify this, Figure 2 (*top panel*) shows radial profiles (averaged over 30° of angle) through the poles (*solid line*) and through the equator (*dashed line*), normalized to the disk temperature of order 10^4 K. There is a slight increase toward the limb in both polar and equatorial profiles, but at the limbs themselves the polar brightening is clearly more than 7%–10% (in absolute values) above the equatorial brightness temperature level. Finally, in Figure 3 we investigate the variation of the brightening around the limb (i.e., as a function of polar angle). The upper panel represents the 17 GHz mean brightness temperature averaged over a radial distance of 50″ just inside the limb, as a function of polar angle measured east from north. The south polar brightening shows up very prominently, while the north polar brightening is present but somewhat less prominent. In both cases the profile is spiky, reflecting the fact that most of the emission is concentrated in discrete compact features.

The polar-cap brightening was present in all microwave images that we studied. As in Figure 1, the polar cap brightening tends to consist of two components: the polar regions beyond 0.9 $R_\odot$ from the disk center showed a weak diffuse component and beyond 0.95 $R_\odot$, patchy unresolved brightenings of higher brightness were almost always present. The compact sources may have been difficult to detect in earlier studies where the spatial resolution was typically 1′. We measure source sizes for the compact features ranging from the beam size of the NRH (about 15″) up to 50″–55″. For a quantitative analysis, we selected the NRH images that were recorded within 1 minute of an EIT image. The

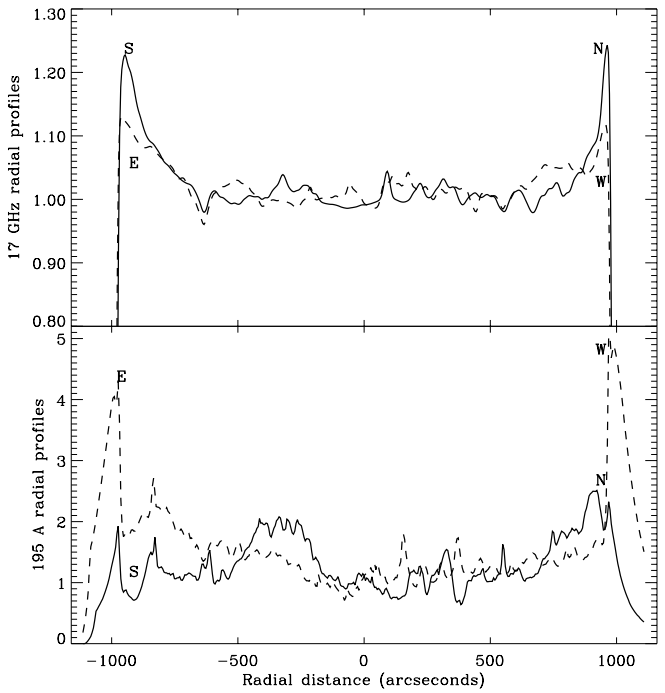

FIG. 2.—Radial profiles in the polar (*solid line*) and equatorial directions (*dashed line*) for the images shown in Fig. 1. The upper panel presents the 17 GHz profiles and the lower panel presents the 195 Å profiles. The profiles are normalized to the mean level on the solar disk (about 10^4 K at 17 GHz) in each case. Each profile represents an average over 15° either side of the pole/equator in 0°.5 steps. The polar coronal holes are marked.

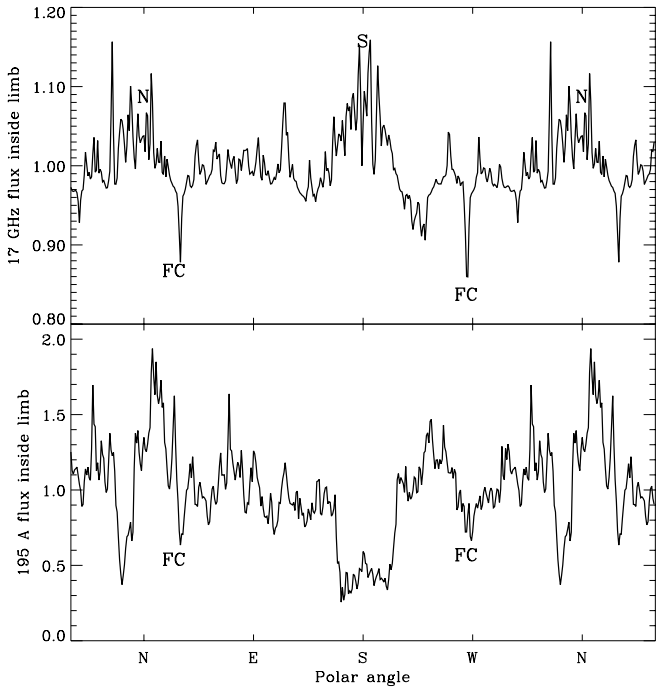

FIG. 3.—Azimuthal profiles of the emission just inside the limb in the images in Fig. 1. The upper panel presents the 17 GHz profile and the lower panel presents the 195 Å profile. The profiles are normalized to the mean level of the profile in each case. The images were averaged over 50″ in the radial direction every 1°, measured east from north. The curve has been wrapped so that the north pole appears at both ends of the profile displayed. The polar coronal holes are marked, as are the locations of depressions corresponding to filament channels ("FC") just inside the limb.

average temperature of the diffuse polar emission was about 11,500 K while the average quiet-Sun disk brightness was 10,000 K, and the detection threshold of the NRH (the 3 σ level of fluctuations in quiet regions of the disk) was approximately 200 K (although it varied somewhat from day to day). Some compact microwave sources reached brightness temperatures as high as 15,500 K, but the average value of their maximum brightness temperatures was 13,500 K.

It is striking that the microwave polar brightening is more prominent at the south pole than at the north (this is shown more clearly in Fig. 4). The south pole was tilted toward us, and as noted by Koshiishi (1996) and Shibasaki (1998), inspection of images covering a range of tilts clearly shows that the tilt angle is an important factor. For example, on 1997 March 19 (Fig. 4) the total average flux of the south pole radio brightening was more than 1.9–2.1 times larger than the corresponding north pole average flux. Shibasaki (1998) showed using synoptic 17 GHz maps that the variation of the polar cap brightening boundaries is roughly sinusoidal, in agreement with the annual variation of the heliographic latitude of the disk center (B_0). The same argument was also used by Kosugi, Ishiguro, & Shibasaki (1986) for the interpretation of the wider radial size of the north polar-cap brightening they observed from 1984 July 16–July 22, (B_0 was about $+5°$). Koshiishi (1996) carried out a detailed study and showed that the area of the polar brightening, the peak brightness in it, and the apparent latitude of the boundary all vary with the apparent yearly solar changes, but not in a perfectly sinusoidal fashion.

4. COMPARISON OF THE MICROWAVE AND EUV POLAR FEATURES

We compared the microwave polar emission with the nearly simultaneous EIT images in the lines of He II at 304 Å and Fe XII at 195 Å. The peak temperature response of the He II line is about 80,000 K, and the compact bright features seen in the 304 Å images are associated with the chromospheric network elements (see Wang et al. 1997). The Fe XII line is coronal (peak temperature response 1.4×10^6 K), and the 195 Å images show clearly the coronal holes as dark areas and also the polar plumes as almost linear diffuse bright features within the coronal holes (e.g., DeForest et al. 1997; DeForest 1998). Figures 1, 2, and 3 show a 195 Å image and the profiles extracted from it, while Figure 4 shows a comparison of the 304 Å emission at the poles with the 17 GHz emission. Figure 2 shows that limb brightening is very prominent at the equator in the 195 Å image, whereas it is very small at the poles. The coronal hole at the south pole is striking in the 195 Å profiles in Figure 2, while the north pole is less prominent: Figure 1 shows that foreground material obscures much of the north polar region from our view, particularly on the eastern side, and this effect can be seen in Figure 3: the 195 Å profile has a large depression corresponding to the south pole but only a small depression at the north pole, while just to the east of the north pole is a bright feature.

For 1997 March 11, we computed a NRH synthesis map using a 2.5 hr long visibility database. By synthesizing images from visibilities that cover more than 2 hr of observations, the *u-v* coverage improves, and therefore the corresponding maps have higher image fidelity than the snapshot maps. We note that the solar differential rotation is not

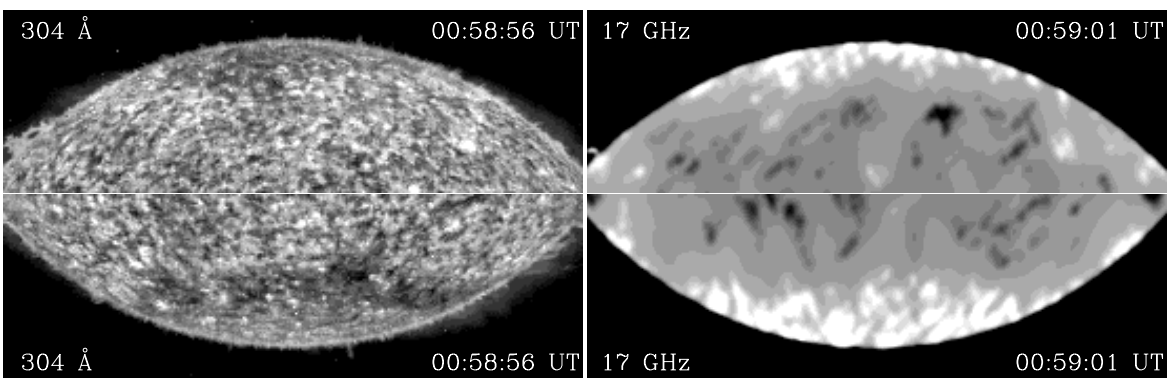

FIG. 4.—EIT images taken in the chromospheric line of He II at 304 Å on 1997 March 19 and the corresponding NRH 17 GHz maps. *Top:* north pole; *bottom:* south pole. The south pole 17 GHz emission is clearly more prominent.

significant for the polar regions we are interested in. For a period of 6 hr, the shift of a polar source located at a latitude of $\pm 85^\circ$ is about 2″, which is very small compared to the beam size. We compared the boundaries of the polar-cap brightening of the synthesis radio image with the boundaries of the 195 Å coronal holes. This method is reliable because it is well known (e.g., see Timothy, Krieger, & Vaiana 1975) that the shape of the coronal holes does not change in such a short time. We found that the boundaries of the polar cap brightening did not match exactly the coronal hole boundaries. The polar brightenings extended well beyond the east border of the coronal hole, in agreement with Figure 3. Figure 3 also indicates that the FWHM of the 17 GHz south polar brightening is about 5° wider in the east-west direction than the EUV south coronal hole. A comparison between the synthesized radio map and the corresponding average He II 304 Å image showed again that the boundaries of the polar brightening did not match exactly the 304 Å boundaries of the coronal hole. Shibasaki (1998) compared NRH and soft X-ray synoptic maps and reached the same conclusion.

Comparison of 17 GHz and EIT images (see Fig. 4) indicates that the patchy radio brightenings do not necessarily correspond to bright 304 Å structures. Specifically, more than 65% of the 17 GHz compact sources did not coincide (in the sense that the overlap of the areas was less than 20%) with bright 304 Å elements. In Figure 5 we present 1 minute cadence snapshot NRH images of the south pole and nearly simultaneous 195 Å EIT images. Again most of the patchy radio brightenings did not correspond to bright 195 Å fea-

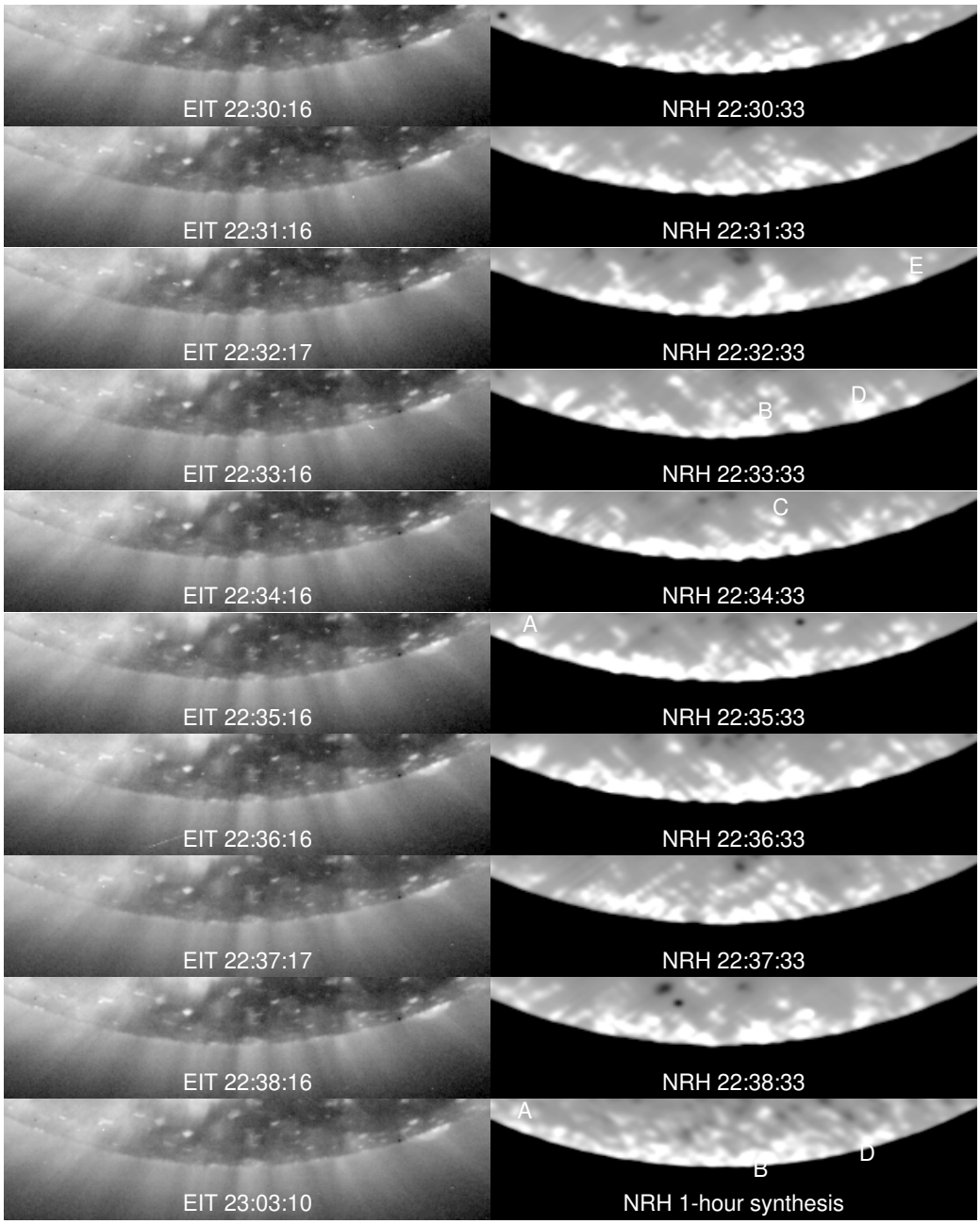

FIG. 5.—Partial-frame mode EIT images taken in the coronal line of Fe XII at 195 Å on 1997 May 29 and the corresponding NRH 17 GHz maps. The bottom NRH image was synthesized using a 1 minute cadence, 1 hr long visibility database (data from 22:30 UT to 23:30 UT). The other NRH images are snapshot images. Note that the EUV emission does not change but the 17 GHz features change considerably.

tures. Using the same criterion, we found that about 70% of the microwave sources were not associated with the 195 Å plume emission. Given the fact that the patterns of the 304 Å polar network brightenings roughly coincide with the base locations of diffuse 195 Å emission (Wang et al., 1997), our results indicate that most of the compact microwave polar sources were associated with the interplume regions.

It is well known (see Wilhelm et al. 1998) that macrospicules are not directly related to plumes. Indeed, some of the strongest macrospicules can be seen in interplume lanes without plume activity. We defined as macrospicules all the collimated emission features seen in the 304 Å images that were more than 15″ above the polar limb (e.g., see Wang 1998). A comparison of our microwave images with the 304 Å images shows that less than 15% of the compact radio features were associated with macrospicules. Apparently, more simultaneous high time-resolution data in radio and EUV wavelengths are needed in order to establish the correlation (or the absence thereof) between the two effects.

An important question is whether the polar brightening is a feature peculiar to the poles or whether it is shared by all coronal holes. To answer this question we should investigate coronal holes near the limb away from the poles, since foreshortening effects associated with being near the limb may be important. We note that there are two features near the limb in Figure 1 (both labeled "FC"), at about 20° east of north and at about 5° south of west, which both show up as strong narrow depressions in the 17 GHz azimuthal profile and as smaller depressions in the 195 Å profile (also labeled "FC" in Fig. 3). However, we have inspected EIT and Big Bear Hα images when these features were on the disk, and we believe that they are actually filaments or filament channels rather than coronal holes (for a statistical study of the microwave emission of Hα filaments, see Schmahl, Bobrowsky, & Kundu 1981). This was also true of other days when similar strong narrow depressions near the limb were present in the 17 GHz images. We note that the basic criterion we used to select the data that we study in this paper was the absence of strong activity and not the presence of coronal holes near the limb, away from the poles. Kosugi et al. (1986) found that at 36 GHz about half of the equatorial coronal holes they observed showed excess brightening. Koshiishi (1996) reports a large number of cases in which coronal holes on the disk show brightening, particularly at the edges of regions where a long coronal hole narrows. Gopalswamy et al. (1998, 1999) present observations of a large "elephant-trunk" coronal hole on 1996 August 26 that shows some evidence for bright 17 GHz emission on the disk in the form of compact features similar to those seen at the poles; they are not as bright as the corresponding polar features seen on the same day, which could be due to the lack of foreshortening effects on the disk. Thus it seems that the radio brightening can occur in low-latitude coronal holes as well as at the poles.

5. TIME VARIABILITY OF THE MICROWAVE AND EUV EMISSION

For analysis of the short-timescale temporal properties of the polar brightening we studied sequences of Nobeyama images such as the sequences of 1 s integration images 1 minute apart on 1997 May 29–30 and June 2 (see Fig. 5 for an example). A preliminary version of the results has been presented by Kundu (1999). When studying the variability of compact features such as these, one has to be careful not to overinterpret the data. The MEM deconvolution algorithm should do a better job than conventional CLEANing at not representing diffuse extended emission as small beam-sized structures, but the results may still be disturbed by sidelobes in the dirty map from other sources. The complex interplay between the NRH response and the MEM algorithm makes it difficult to separate real features and their temporal variation from false ones. Below we describe the characteristics of those sources that we believe are the best candidates for real sources based on their brightness and longevity. However, we caution the reader that the conclusions of this section remain uncertain owing to the complexity of the image restoration problem and the apparent lack of correlation of the microwave sources with EUV sources. Koshiishi (1996) considered the problem of the reality of the compact features in detail and showed that some of them are longer-lived and clearly real. For weak, shorter-lived features it is even more difficult to distinguish the fluctuations from sidelobes. Some of the short-lived features are the brightest features in the poles and well above the noise level. However, this does not necessarily mean that they are real because sidelobes can overlap and give peaks that are greater than one might expect from the sidelobe level for a single source. Figure 5 (*right column*) shows several changes from frame to frame but also provides examples of bright sources that are clearly present in at least two successive frames and are probably real. Source A is present at 22:34 UT; for the next two minutes its intensity increases, and then it decays. The source that is under the letter B can be identified from 22:33 UT till 22:38 UT. Source C appears weak and diffuse at 22:33 UT, its intensity increases significantly at 22:34 and for the next two minutes, it decays. Sources D and E are present in almost all frames that we show. The images indicate that both sources recur. Comparisons between synthesis maps made by 1 hr long visibility databases and snapshot maps made by the constituent time stamps of such visibilities are also useful. Polar features that are present in snapshot maps and survive in the 1 hr synthesis map are probably real. Such examples are presented in Figure 5. Sources, A, B, and D, which were identified in more than one snapshot map, are also present in the 1 hr synthesis map. The lifetimes of the sources that show in 1 hr synthesis images are not necessarily 1 hr; the sources may survive because they recur in fixed positions even though their lifetimes are much shorter. This is clearly the case for sources A and D of Figure 5.

We also inspected a 7 minute cadence, 6 hr long sequence of NRH images taken on 1997 March 19. In parts of that sequence of images, the compact features seem "to dance around" and not to be the same from frame to frame. An example from the 7 minute cadence 1997 March data is presented in Figure 6. No sources in Figure 6 (with the exception of source G, which shows up in all frames of the figure) are the same between the 03:37 UT image and the 03:44 UT image. In other parts of the sequence, however, there are polar sources that are present in at least two successive frames. In Figure 6, for example, almost all sources that are present at 03:51 UT also appear in the 03:58 UT image, even though the intensities and shapes of most of them have changed. NRH maps averaged over 1 hr or longer show compact features corresponding to some of the brighter sources, but otherwise the emission is smooth. Thus it seems that the lifetimes of most of the sources should be less than 7 minutes, but there are also some

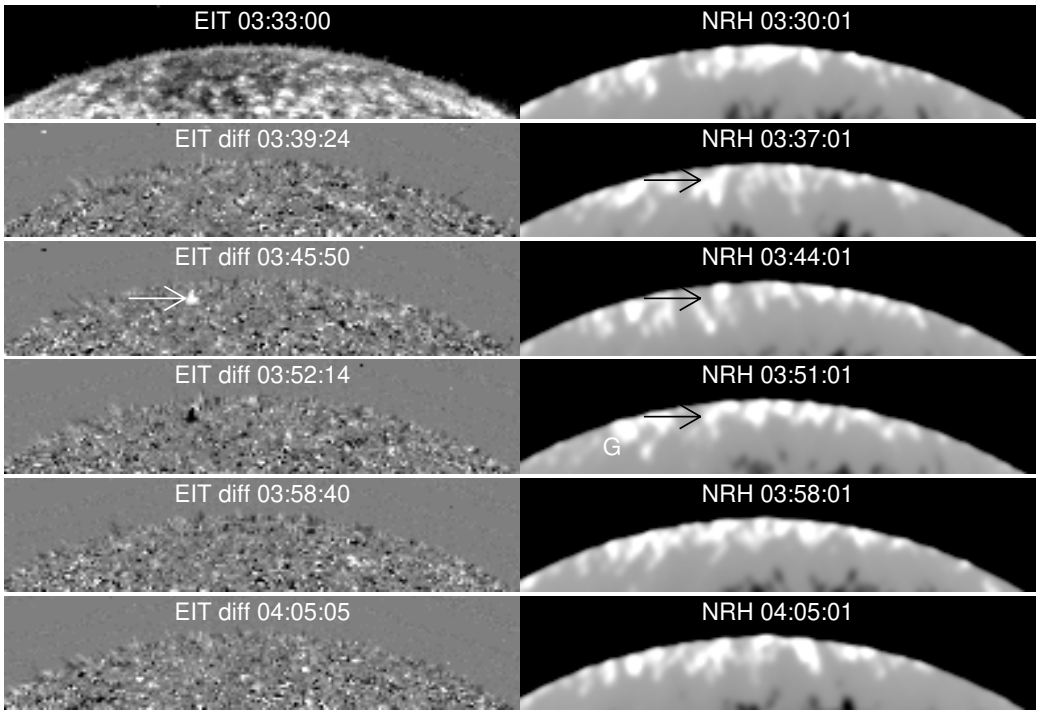

FIG. 6.—EIT images taken in the chromospheric line of He II at 304 Å on 1997 March 19 and the corresponding NRH 17 GHz maps. All but the first of the EIT images are presented as running difference images. The microwave polar sources change considerably, but these changes did not correspond to changes in the EUV emission. On the other hand, a changing 304 Å feature (indicated by the arrow) was associated with the diffuse component of the microwave polar brightening, which was practically constant. The black arrows on the NRH images have been plotted on the same locations as the white arrow.

sources that live longer. However, we note that these results are subject to great uncertainties because what we observed could reflect, at least partly, properties of the sidelobes and not of real sources. If the emission is dominated by short-lived features, then they must be capable of occurring over much of the polar region.

We also looked for the correlation (or the absence thereof) between the temporal variations of the microwave emission and changing features as seen from EIT images for the 1997 March 19, May 29–30, and June 2 data. A "macropixel" analysis (for details on the method see Shimizu 1995; Shimizu & Tsuneta 1997) was applied to both the NRH and EIT maps. The NRH images were divided into macropixels, each one consisting of 3×3 original pixels. Any intensity enhancement above the 7 σ level from the background radio emission was considered as one of the compact polar sources. The EIT images were interpolated so that their macropixel size was equal to the NRH macropixel size. Less than 2% of the compact microwave sources were associated with changes of the corresponding 304 Å emission, which were higher than the 3 σ level above the EUV background. The macropixel analysis is consistent with the visual inspection of the data, which shows that the compact radio sources were not associated with bright changing 304 Å network structures. In Figure 6 the bright microwave sources have changed significantly over 35 minutes: new sources appeared and others dimmed into the diffuse polar brightening. Even from frame to frame, the microwave emission of most polar sources fluctuated considerably. However, Figure 6 shows that these changes did not correspond to changes in the EUV emission. On the other hand, almost all changing 304 Å features (peaks above 5–7 σ from background; an example is indicated by the arrow in Fig. 6) were associated with the diffuse component of the microwave polar brightening, which was practically constant. Of course, the 304 Å brightenings may produce microwave emission that is below the detection threshold of the NRH. Using the high-cadence data (1 minute) of 1997 May 29–30 and June 2 we confirmed the above results: the fluctuations of radio emission did not correspond to changes of the 195 Å emission, which was especially quiet (see Fig. 5).

Studying high-cadence NRH images, we have been able to show that some of the compact polar sources were real. This was also confirmed by comparisons between synthesis maps made by 1 hr long visibility databases and snapshot maps made by the constituent time stamps of such visibilities. An important question that needs to be answered is whether we can develop a more general criterion to distinguish between the real polar sources and the ones that are sidelobes from other sources. Unfortunately we cannot use the EIT data for this purpose because of the overall lack of correlation between the radio and EUV polar data. As a first approximation we can consider as not real all sources that appear in only one image of a 1 minute cadence NRH sequence of images. Sources that show weak diffuse elongated "tails" also may not be real in most cases because the tails reflect the presence of sidelobes of the solar limbs. Structures that are not real are expected to move as the sidelobes rotate with time (Koshiishi 1996). In order to identify the moving features, we applied the standard local correlation tracking technique (November & Simon 1988) to the NRH data. We made several tests using different sizes of sampling windows and time intervals between successive frames. However, the velocity fields that we computed did not always agree with visual inspection of the NRH movies.

This is not surprising because the correlation tracking technique works reasonably well when it handles organized velocity patterns. In our cases, the visual inspection of the data did not reveal such patterns. However, as expected, all sources that we identified as real corresponded to practically insignificant velocities in agreement with the visual inspection of the data.

6. DISCUSSION AND CONCLUSIONS

We have studied the properties of polar-cap brightening using 17 GHz images from NRH. The polar brightening consists of a diffuse component of about 1500 K average excess-brightness temperatures and compact patchy sources of excess brightness more than 3000 K. If the polar brightening comes from optically thin free-free radiation, then local enhancements of electron density by a factor of 1.4 are needed in order to reproduce the contrast between the compact sources and the diffuse component of the polar brightening.

We compared the microwave polar emission with the corresponding *SOHO*/EIT images at 304 and 195 Å. Most microwave patchy sources (more than 65%) did not correspond either to bright 304 Å structures or to bright 195 Å features (coronal hole polar plumes). Most of these compact radio sources were associated with the interplume regions, which are thought to be the sources of the high-speed polar wind (Wang et al. 1997; Wilhelm et al. 1998). The calculation of the average NRH images as well as the production of synthesis images using 2 hr long visibility data sets reduce the level of sidelobe patterns compared to sidelobe level of snapshot maps. A comparison between the average EIT images and average/synthesized NRH images confirms that most of the microwave sources that survived were still not associated with bright EUV features. Thus, this effect cannot be exclusively an artifact of the deconvolution method. The lack of good correlation between the compact microwave sources and the bright polar EUV 195 Å coronal features on either long or short timescales, (except of course for the fact that the 17 GHz brightenings occur in the polar coronal holes visible in the EIT images) might suggest that the brightenings are not at coronal temperatures. A number of other arguments support this conclusion:

1. The absence of correlation between most of the microwave polar sources and the bright 304 Å network elements suggests that the bulk radio emission of these sources comes from heights below the 80,000 K layer, which is the temperature of the maximum fractional abundance of He II at 304 Å.

2. The bright radio features never appear above the 17 GHz polar limb, which is at a height of 8700 km above the photosphere. This implies that they have a small-scale height and therefore consist of cool material. Note that since the brightness temperature of the disk at 17 GHz is 10^4 K, the atmosphere is optically thin down to the chromosphere and any material at temperatures of this order or above can contribute to the brightenings, in contrast to the EIT images, which are only sensitive to much hotter material.

3. An additional argument for a small-scale height is the strong dependence on the solar tilt angle: the total flux and number of compact radio sources as well as the north-south radial extent of the diffuse polar brightening are clearly larger in the pole that is closer to the Earth (Koshiishi 1996; Shibasaki 1998). If the sources are coronal, then the density scale height for electron temperature 10^6 K and mean atomic weight 1.4 would be about 0.14 $R_\odot$. However, a source 7° behind the limb is only 0.0075 $R_\odot$ (one–twentieth of a scale height) below the line of sight through the limb, i.e., any hot material associated with such a feature should appear above the limb and the dependence on tilt angle would be very weak.

4. Further, the radio polar brightenings lie below the 304 Å limb that corresponds to the upper envelope of plasma at 8×10^4 K.

We therefore suggest that the radio polar brightenings are due to very cool material ejected into the polar atmosphere on open field lines in a predominantly transient fashion. The lack of correlation with 304 Å features implies that the temperature of material is below 8×10^4 K, and therefore suggests that we investigate the association between the transient features and UV observations of the poles.

Our data show that the 17 GHz polar features change significantly with time. While some weak short-lived features (lifetimes about 1 minute) are difficult to distinguish from sidelobes, some others live longer, do not move, and are probably real sources. We have shown that the changes in radio emission do not correspond to changes in the EUV polar emission. This result clearly rules out our earlier speculation that the excess polar radio brightening may reflect the summation of random EUV brightenings associated with plume and/or interplume regions. Of course, we cannot exclude the possibility that there are such brightenings that last less than the time resolution of the EIT data. However, this is not very likely because the 1 minute cadence 195 Å movies that we studied showed that the EUV emission was practically stable, and even if there were such extremely short-lived EUV features, some of them would have shown up in the images if they occurred in a semi-continuous way.

This research at the University of Maryland was carried out with support from NSF grants ATM 96-12738 and INT 97-22489 and NASA grant NAG 5-6257. We acknowledge the essential work carried out by Tim Bastian, Kiyoto Shibasaki, and Shinzo Enome in making it possible to import calibrated Nobeyama data into AIPS. Without their efforts, this analysis and the comparison of different deconvolution techniques on NRH data would have been much more difficult. D. E. G. was supported by NSF grant ATM 97-96213 and NASA grant NAG 5-6381 to New Jersey Institute of Technology.

APPENDIX

DECONVOLUTION OF NRH MAPS

In order to study the reality of the compact polar sources, we compared snapshot full-disk maps produced by different restoration techniques. The raw NRH data were calibrated and imported into AIPS (processing in AIPS follows a path

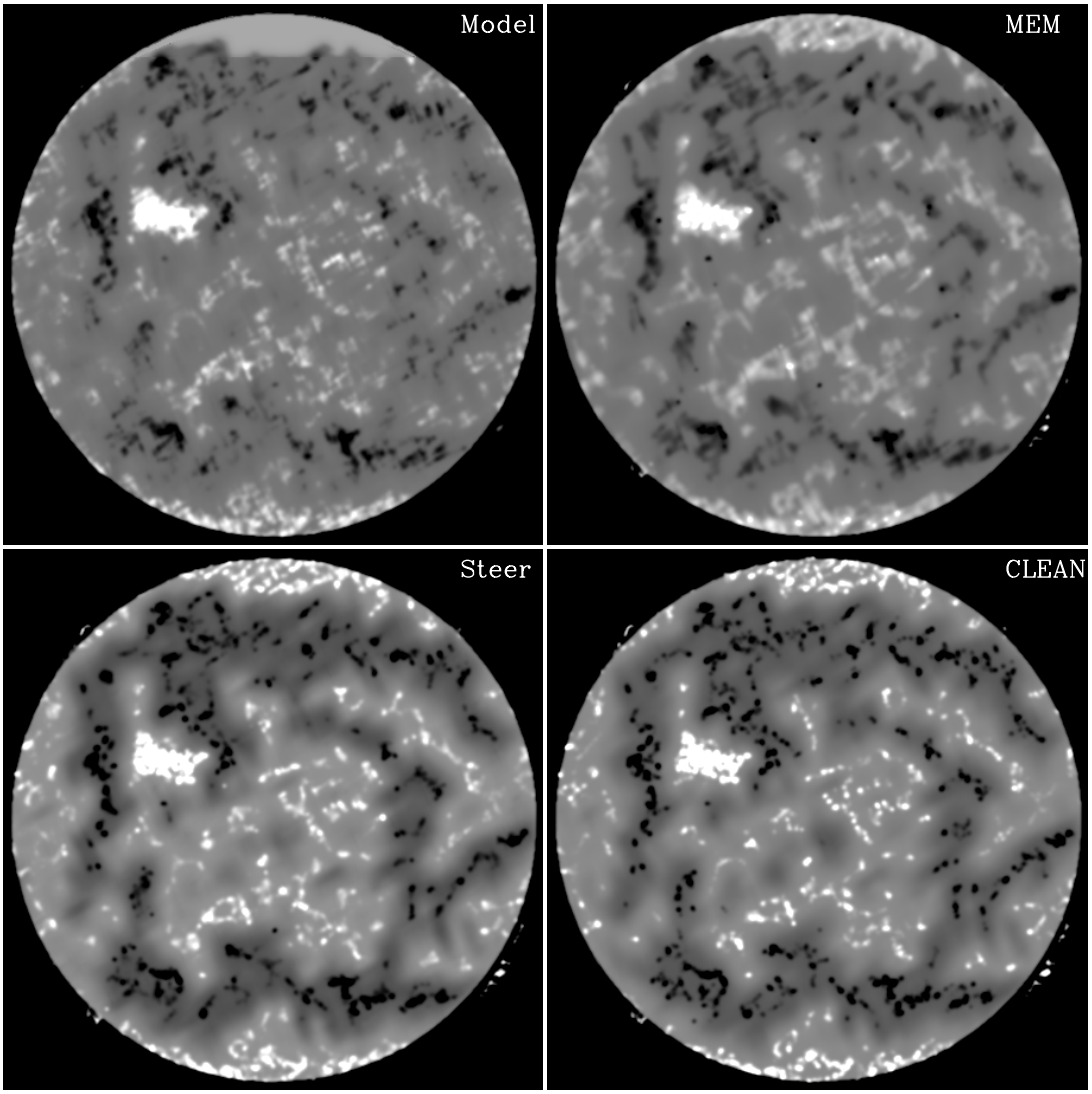

FIG. 7.—The input map that produced the model visibility (*top left*, see text for details) and the resulting final model maps made with different deconvolution techniques. *Top right:* Maximum entropy method map; *bottom left:* Steer CLEAN map; *bottom right:* standard CLEAN map.

developed by Tim Bastian; Bastian, Enome, & Shibasaki 1999). After rectifying a polarization offset and correcting for instrumental gain variations and image motion, we modeled and subtracted the background disk from the data. We mapped each resulting time stamp (i.e., visibility data base for a given time) and removed bright emission with a shallow "CLEAN." The CLEAN components were then subtracted from each time stamp. The residual data can be treated using a variety of mapping and deconvolution techniques. We note that all three techniques that we used were applied effectively to the same dirty maps of the residual emission. We tried the standard CLEAN algorithm with a loop gain of 0.05 (experience shows that extended structure is represented somewhat better in CLEAN maps made with low loop gains; on the other hand, the improvements in deconvolution for loop gains much lower than 0.01 are usually minimal). Subsequently, we tried the so-called Steer CLEAN algorithm (Steer et al. 1984). This method does not remove individual components but groups of components, which are chosen by including all those points in the residual map that rise above a contour set at some fraction of the peak level (the "trim level"). The number of pixels to be subtracted in one iteration increases when the trim level is low. A very high trim level is equivalent to the standard CLEAN. On the other hand, if the trim level is too low, sidelobe features may incorrectly included as components. Our tests showed that the best Steer maps were produced with a trim level of 0.8, which is also the value used by Koshiishi (1996). Finally, we used MEM as embodied in the AIPS task UTESS; the more commonly used VTESS task cannot be used because it incorporates a positivity constraint that is not appropriate for disk-subtracted images. Finally, both the background disk and the clean components of the bright emission were added back and combined with the final residual map. We note that we mapped the visibilities using uniform weighting, which yields higher spatial resolution and lower sidelobes than natural weighting at the expense of slightly reduced sensitivity. Our experiments with natural weighting often produced erroneous features on the maps: a faint pattern of repeated stripes was present on some Steer maps. That pattern was absent when we processed the same data again using uniform weighting and the Steer method and we assume that the errors were due to the larger sidelobes of the naturally weighted beam.

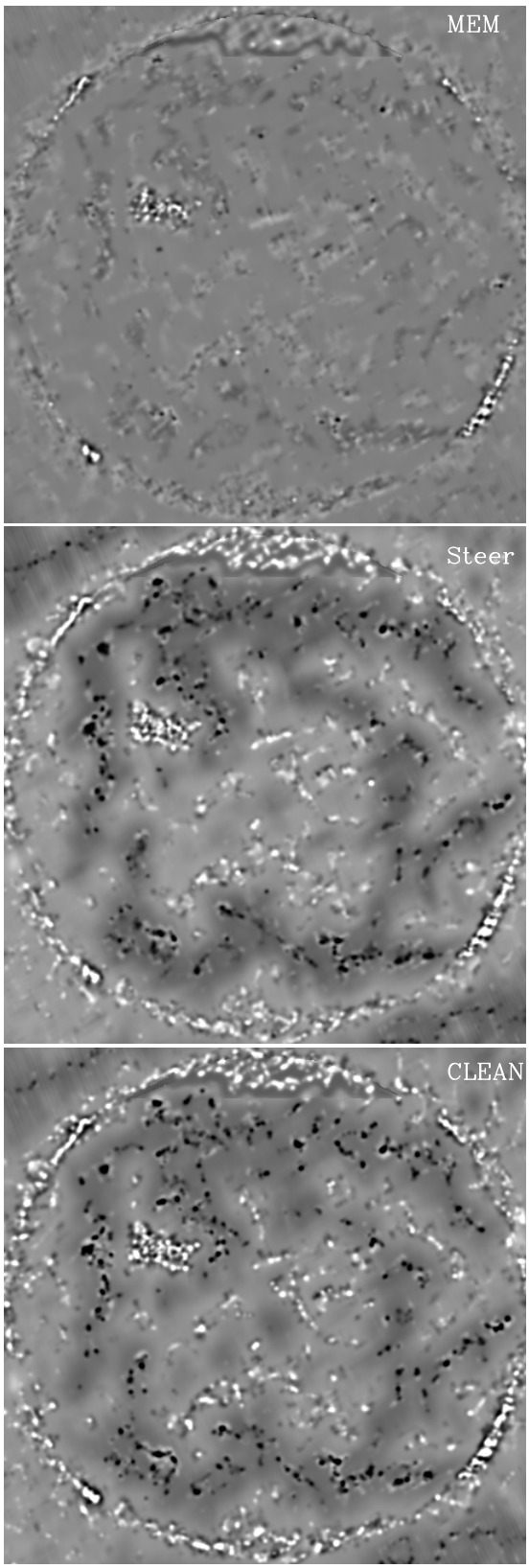

FIG. 8.—Difference images between the final model maps presented in Fig. 7 and the input model map. *From top to bottom:* MEM, Steer CLEAN, and standard CLEAN difference images. Note that the gray-scale range is from −2000 K to 2000 K in all difference images.

The final maps using the three different deconvolution methods were different with the standard CLEAN map being blotchy and the MEM map much smoother. Since the three maps were not identical, the most important question that needs to be answered is which one was closer to the correct image. In order to tackle this question, as well as to investigate the reality of the compact sources in the polar regions of the three different maps, we produced a model visibility database by convolving the original *u-v* samples with a model image (AIPS task UVSUB). The model image (Fig. 7, *top left*) was derived from actual data, but we replaced all points of its north polar region that were above 10,000 K with a smooth intensity of about 11,000 K and smoothed the south border of the 11,000 K region with a 15″ × 15″ beam. This allows us to compare how the different deconvolution methods handle blotchy and smooth regions of similar total flux. The model visibilities were processed as above, and three model maps were made using MEM, Steer CLEAN, and standard CLEAN (Fig. 7, *top right and bottom panels*).

The overall appearance of the three model maps is similar to the corresponding maps, which were produced from the original NRH data. A visual inspection of Figure 7 shows that the standard CLEAN map is blotchy with bright and dark unresolved "spots" all over the disk. The Steer map is somewhat less blotchy but not qualitatively different from the standard CLEAN map, while the MEM map is significantly smoother. These differences reflect the differences in the deconvolution schemes. The standard CLEAN method tries to model radio emission by a number of point sources. The Steer method should do a better job than conventional cleaning at not representing diffuse extended sources as small beam-sized structures because it removes components in groups rather than individually. MEM incorporates a smoothness constraint; it will only tend to produce small features if the data are not consistent with smooth emission. The rms noise levels of the model maps are 750, 680, and 432 K for the standard CLEAN, Steer CLEAN, and MEM maps, respectively.

The extended emission of the north polar region of the input model map is not recovered in the CLEAN or Steer maps: in both of them, much of the continuous emission has been decomposed into small discrete sources. On the other hand, the corresponding region of the final MEM map is much smoother and the bulk of the extended emission is still present, although there are some erroneous features that have been introduced by deconvolution. The different properties of the restoration techniques are also illustrated in Figure 8, where we present the difference images between the final model maps and the input model (note that the gray-scale range of the three difference images is the same). The difference images show clearly that the MEM map is much closer to the correct image than the two CLEAN images. They also confirm that the mottled features that dominate the CLEAN images are due to the failure of CLEAN to reconstruct accurately extended diffuse sources. This effect is prominent in the north polar regions of the difference images. The rms noise in the north polar region is 287, 610, and 675 K for the MEM, Steer CLEAN, and standard CLEAN difference image, respectively. It is also noteworthy that the CLEAN and Steer difference images contain errors on larger spatial scales that are less pronounced in the MEM image and which dominate the noise in the difference images. Our modeling indicates that much of the compact structure that appears in polar regions of NRH maps made by CLEAN is not trustworthy and that it may be, in part, the result of the poor performance of CLEAN on extended sources. MEM did a much better job on the extended emission of the north pole, and therefore the reliability of the fine structure that is present in MEM polar regions is significantly higher.

REFERENCES

Babin, A. N., Gopasyuk, S. I., Efanov, V. A., Kotov, V. A., Moiseev, I. G., & Tsap, T. T. 1976, Izv. Krymskoi Astrofiz. Obs., 55, 3
Bastian, T. S., Enome, S., & Shibasaki, K. 1999, in preparation
Berghmans, D., Clette, F., & Moses, D. 1998, A&A, 336, 1039
DeForest, C. E. 1998, in Solar Jets and Coronal Plumes, ed. S. Koutchmy, P. Martens, & K. Shibata (ESA SP 421; Noordwijk: ESA), 63
DeForest, C. E., & Gurman, J. B. 1998, ApJ, 501, L217
DeForest, C. E., et al. 1997, Sol. Phys., 175, 393
Delaboudinière, J.-P., et al. 1995, Sol. Phys., 162, 291
Efanov, V. A., Labrum, N., Moiseev, I. G., Nesterov, N. S., & Steward, R. T. 1980a, Izv. Krymskoi Astrofiz. Obs., 61, 52
Efanov, V. A., Moiseev, I. G., Nesterov, N. S., & Steward, R. T. 1980b, in IAU Symp. 86, Radio Physics of the Sun, ed. M. R. Kundu & T. Gergely (Dordrecht: Reidel), 141
Gopalsamy, N., Shibasaki, N., DeForest, C. E., Bromage, B. J. I., & Del Zanna, G. 1998, in ASP Conf. Ser. 140, Synoptic Solar Physics, ed. K. S. Balasubramanian, J. W. Harvey, & D. M. Rabin (San Francisco: ASP), 363
Gopalsamy, N., Shibasaki, N., Thompson, B. J., Gurman, J., & DeForest, C. 1999, J. Geophys. Res., 104, 9767
Hiei, E. 1987, PASJ, 39, 937
Johannesson, A., & Zirin, H. 1996, ApJ, 471, 510
Koshiishi, H. 1996, Ph.D. Thesis, Univ. Tokyo
Koshiishi, H., et al. 1994, PASJ, 46, L33
Kosugi, T., Ishiguro, M., & Shibasaki, K. 1986, PASJ, 38, 1
Kundu, M. R. 1999, in Nobeyama Symposium on Solar Physics with Radio Observations, ed. T. S. Bastian, N. Gopalswamy, & K. Shibasaki, K., in press
Kundu, M. R., & McCullough, T. P. 1972, Sol. Phys., 24, 133
November, L. J., & Simon, G. W. 1988, ApJ, 333, 427
Pohjolainen, S., Portier-Fozani, F., Ragaigne, D., & Heikkila, J. 1998, in CESRA Workshop on Coronal Explosive Events, Metsaehovi Publications on Radio Science
Riehokainen, A., Urpo, S., & Valtaoja, E. 1998, A&A, 333, 741
Schmahl, E. J., Bobrowsky, M., & Kundu, M. R. 1981, Sol. Phys., 71, 311
Shibasaki, K. 1998, in in ASP Conf. Ser. 140, Synoptic Solar Physics, ed. K. S. Balasubramanian, J. W. Harvey, & D. M. Rabin (San Francisco: ASP), 373
Shimizu, T. 1995, PASJ, 47, 251
Shimizu, T., & Tsuneta, S. 1997, ApJ, 486, 1045
Steer, D. G., Dewdney, P. E., & Ito, M. R. 1984, A&A, 137, 159
Timothy, A. F., Krieger, A. S., & Vaiana, G. S. 1975, Sol. Phys., 42, 135
Wang, H. 1998, ApJ, 509, 461
Wang, Y.-M., et al. 1997, ApJ, 484, L75
Wilhelm, K., et al. 1998, ApJ, 500, 1023
Zhang, J., White, S. M., & Kundu, M. R. 1998, ApJ, 504, L127